



OPEN

Graphene oxide electrocatalyst on MnO₂ air cathode as an efficient electron pump for enhanced oxygen reduction in alkaline solution

SUBJECT AREAS:
ELECTROCATALYSIS
ELECTRONIC PROPERTIES AND
DEVICES

Received
23 October 2014

Accepted
17 February 2015

Published
13 March 2015

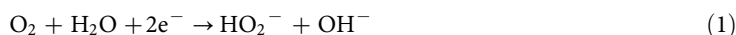
Wan Jeffrey Basirun², Mehran Sookhakistan¹, Saeid Baradaran¹, Zulkarnain Endut⁶,
Mohammad Reza Mahmoudian³, Mehdi Ebadi⁴, Ramin Yousefi⁵, Hanieh Ghadimi¹ & Sohail Ahmed¹

¹Department of Chemistry, University Malaya, Kuala Lumpur 50603, Malaysia, ²Institute of Nanotechnology & Catalysis (NanoCat), University Malaya, 50603 Kuala Lumpur, Malaysia, ³Department of Chemistry, Shahid Sherafat, University of Farhangian, 15916, Tehran, Iran, ⁴Department of Chemistry, Faculty of Sciences, Islamic Azad University, Gorgan, 49147-39975 Iran, ⁵Department of Physics, Masjed-Soleiman Branch, Islamic Azad University, Masjed-Soleiman, Iran, ⁶Center of Foundation Studies, Faculty of Science, Universiti Putra Malaysia, 43400 UPM Serdang, Selangor, Malaysia.

Correspondence and requests for materials should be addressed to W.J.B. (jeff@um.edu.my)

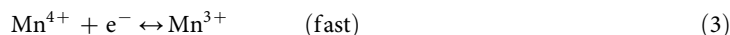
Graphene oxide (GO) was deposited on the surface of a MnO₂ air cathode by thermal evaporation at 50 °C from a GO colloidal suspension. Fourier transformed infrared spectroscopy and field emission scanning electron microscopy confirmed the presence of GO on the MnO₂ air cathode (GO-MnO₂). Voltammetry and chrono-amperometry showed increased currents for the oxygen reduction reaction (ORR) in 6 M KOH solution for GO-MnO₂ compared to the MnO₂ cathode. The GO-MnO₂ was used as an air cathode in an alkaline tin-air cell and produced a maximum power density of 13 mW cm⁻², in contrast to MnO₂, which produced a maximum power density of 9.2 mW cm⁻². The electrochemical impedance spectroscopy results suggest that the chemical step for the ORR is the rate determining step, as proposed earlier by different researchers. It is suggested that the presence of GO and electrochemically reduced graphene oxide (ERGO) on the MnO₂ surface are responsible for the increased rate of this step, whereby GO and ERGO accelerate the process of electron donation to the MnO₂ and to adsorbed oxygen atoms.

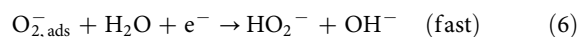
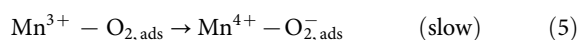
The oxygen reduction reaction (ORR) is one of the most widely studied reactions, particularly for fuel cell and metal-air battery applications. Due to the slow kinetics of the ORR, several materials have been developed as electro-catalysts to accelerate the reaction. Different types of graphene, such as graphene nanosheets¹ and porous graphene² are good electro-catalysts for ORR in lithium-air cells. Graphene-based materials such as nitrogen doped graphene³ and graphene-based Fe-N-C materials⁴ are also important electro-catalyst for the ORR. The most widely used electro-catalyst for the ORR is MnO₂ due to its low cost and high electro-catalytic activity^{5,6}. In alkaline solution, the ORR proceeds with a 4 electron reduction pathway for MnO₂⁵⁻⁷ and graphene^{4,8}. The mechanism of the ORR on electro-catalytic MnO₂ has been studied extensively but is not fully understood. Generally, the ORR in alkaline solutions involves a two-step process and can be given by eq. 1 and eq. 2^{5-7,9}:



The combination of eq. 1 and eq. 2 gives an overall 4 electron reduction for the ORR in alkaline solution.

A detailed mechanism for the first step (eq. 1) on MnO₂ in alkaline medium has been proposed^{7,9}:





$\text{O}_{2,\text{ads}}$ refers to adsorbed oxygen molecules on the MnO_2 surface. The slowest step in the whole process is eq. 5, where electrons received by MnO_2 in eq. 3 are excited and donated to the adsorbed oxygen molecule $\text{O}_{2,\text{ads}}$. Although graphene materials are also good electro-catalyst for the ORR, the superior performance of MnO_2 remains unchallenged by any pure graphene materials. Recently Yang et al.¹⁰ used MnO_2 -graphene nanosheets as the air cathode in lithium-air cells and obtained a discharge capacity much higher than pure graphene nanosheets (GNS) catalyst. On the other hand, pure MnO_2 has lower performance toward the ORR, compared to composites of MnO_2 and graphene materials. Wen et al.¹¹ used MnO_2 -graphene nanosheet composites as the air cathode in microbial fuel cells (MFC) and obtained a power density higher than a pure MnO_2 catalyst. Gnanakumar et al.¹² used nanotubular MnO_2 -GO composites as the air cathode in MFC and obtained a power density higher than the pure MnO_2 nanorods and MnO_2 nanotubes. Qian et al.¹³ also obtained larger voltammetric currents for ORR with MnO_2 /reduced graphene oxide (RGO) composites compared to pure RGO in alkaline solution and also showed that the MnO_2 -RGO composite proceeds with a 4 electron reduction pathway for the ORR. In this work, the formation of stacked graphene oxide (GO) layers on a MnO_2 air cathode and their electro-catalytic performance in an alkaline tin-air cell are investigated.

Results

Figure 1a shows the CV for the first cycle of the electrochemical reduction of GO suspension in 0.1 M phosphate buffer solution, on the MnO_2 substrate. The first anodic wave at around -0.4 V to -0.8 V and the second wave beyond -1.0 V are attributed to the redox pair of oxygen-containing groups on the graphene plane^{14,15}. Figure 1b shows all four cycles for the reduction of GO to ERGO on the MnO_2 substrate. It can be observed that the currents became

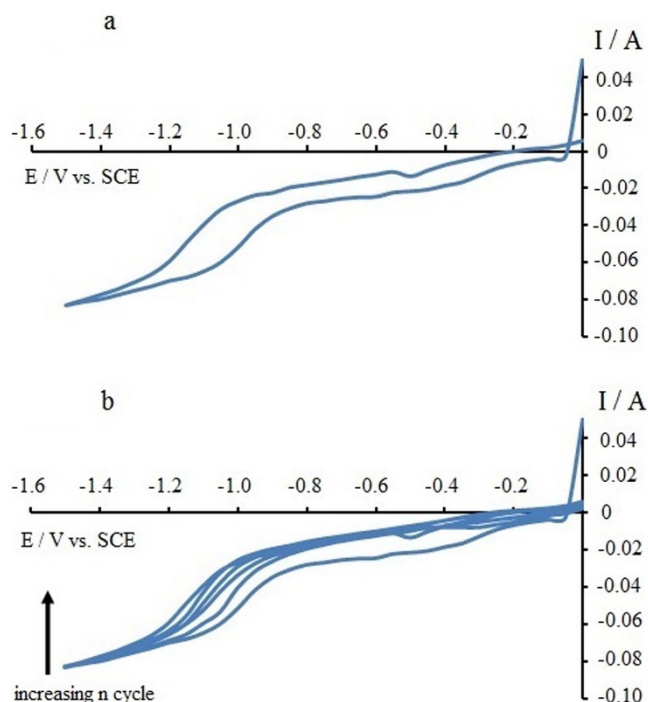


Figure 1 | The CV for the electrochemical reduction of GO onto MnO_2 substrate, (a) first cycle (b) all four cycles.

smaller with increasing cycle numbers. These results are also consistent with previous results on the electro-reduction of GO onto polypyrrole nano-fibers¹⁶. Figure 2a shows the FTIR spectrum of the synthesized GO. All of the characteristic peaks for OH, C=O, C=C, C-OH and C-O are present at approximately 3400, 1730, 1630, 1230 and 1070 cm^{-1} , respectively, in the GO spectrum. Figure 2b is the FTIR spectrum of the GO- MnO_2 air cathode, where the peaks for OH, C=O, C=C and C-OH are still present. The peaks at 2950 and 2870 cm^{-1} are due to the CH_2 and CH vibrations, respectively, from the carbon black additive in the MnO_2 air cathode¹⁷. Due to the thermal evaporation of the GO- MnO_2 air cathode, the OH peak at approximately 3400 cm^{-1} becomes smaller compared to the C=O and C=C peaks in the FTIR spectrum in Fig. 2b. In Figs. 2b and 2c, the bands at *p*, *q*, *r*, *s* and *t* are due to the MnO_2 substrate layer. The band at approximately 2700 cm^{-1} (*p*) is due to the fundamental OH stretching with an OH-O length of approximately 2.60 Å in the MnO structure¹⁸. The peak at approximately 2100 cm^{-1} (*q*) is due to the combination of the OH stretching mode at 2700 cm^{-1} and the excited lattice mode at approximately 600 cm^{-1} , where 2700 - 600 = 2100 cm^{-1} , and is very close to previous reports^{19,20}. The peaks at approximately 1550 and 1360 cm^{-1} (*r* and *s*, respectively) are attributed to the interaction of Mn with surrounding species such as OH and O^{2-} . The peak at approximately 1200 cm^{-1} (*t*) is due to the vibration of the hydrated MnO_2 ²¹. The peaks at approximately 1550 and 1360 cm^{-1} (*r* and *s*, respectively), which are due to the interaction of Mn with OH, are evident in Fig. 2c (GO- MnO_2 , after discharge, not dried) compared to Fig. 2b (GO- MnO_2 , before discharge, dried).

Figure 2c is the FTIR spectrum of the GO- MnO_2 after cell discharge, not dried. Figure 2c shows that the C=O peak height, at approximately 1730 cm^{-1} , decreases in the FTIR spectrum of GO- MnO_2 after discharge, compared to Fig. 2b. In Fig. 2b, the C=O peak height at 1730 cm^{-1} is larger than the C-OH peak height at 1230 cm^{-1} . However, in Fig. 2c, the C-OH peak height is larger than the C=O peak, which also suggests that the carbonyl groups were electrochemically reduced during the discharge of the GO- MnO_2 air cathode. Due to the close proximity with the *r* peak, it is unclear whether the C=C peak at approximately 1630 cm^{-1} is slightly decreased in Fig. 2c (GO- MnO_2 , after discharge, not dried), compared to Fig. 2b.

The CH_2 and CH vibrations at 2950 and 2870 cm^{-1} , respectively, in Fig. 2b have lower peak heights compared to C=O at 1730 cm^{-1} . However, in Fig. 2c, the CH_2 and CH vibrations have larger peak heights compared to the C=O peak. This difference could be due to the reduction of the peripheral COOH, (the Lef-Klinowski model²²) to CH_2OH during cell discharge. The bands approximately 1800–2000 cm^{-1} are attributed to the coupling and overtone bands of the aromatic C-H out of plane bending vibration modes^{23,24}. These bands at approximately 1800–2000 cm^{-1} are also present in Fig. 2b and are attributed to the carbon black additive in the MnO_2 ¹⁷. The XPS spectrum of the ERGO electrodeposited on MnO_2 (ERGO- MnO_2) is shown in Fig. 2d, and resembles the XPS of the GO- MnO_2 after discharge (Fig. 2c)

The FESEM images (supplementary information Figure SI-1) of the MnO_2 and GO- MnO_2 and ERGO- MnO_2 air cathode surfaces show that the GO and ERGO flat sheets are stacked on one another on the MnO_2 substrate, where GO has only partial surface coverage on the MnO_2 substrate. It can be observed that GO has sheet morphology, whereas MnO_2 has grain morphology due to the preparation methods described in the experimental section.

X-ray photoelectron spectroscopy. The XPS spectra of the C 1s binding energy for GO- MnO_2 before discharge, dried, and GO- MnO_2 after discharge, not dried are shown in the supporting information (SI-2a and SI-2b). The binding energies at 284.5 eV and 284.6 eV (SI-2a and SI-2b, respectively), are attributed to C-

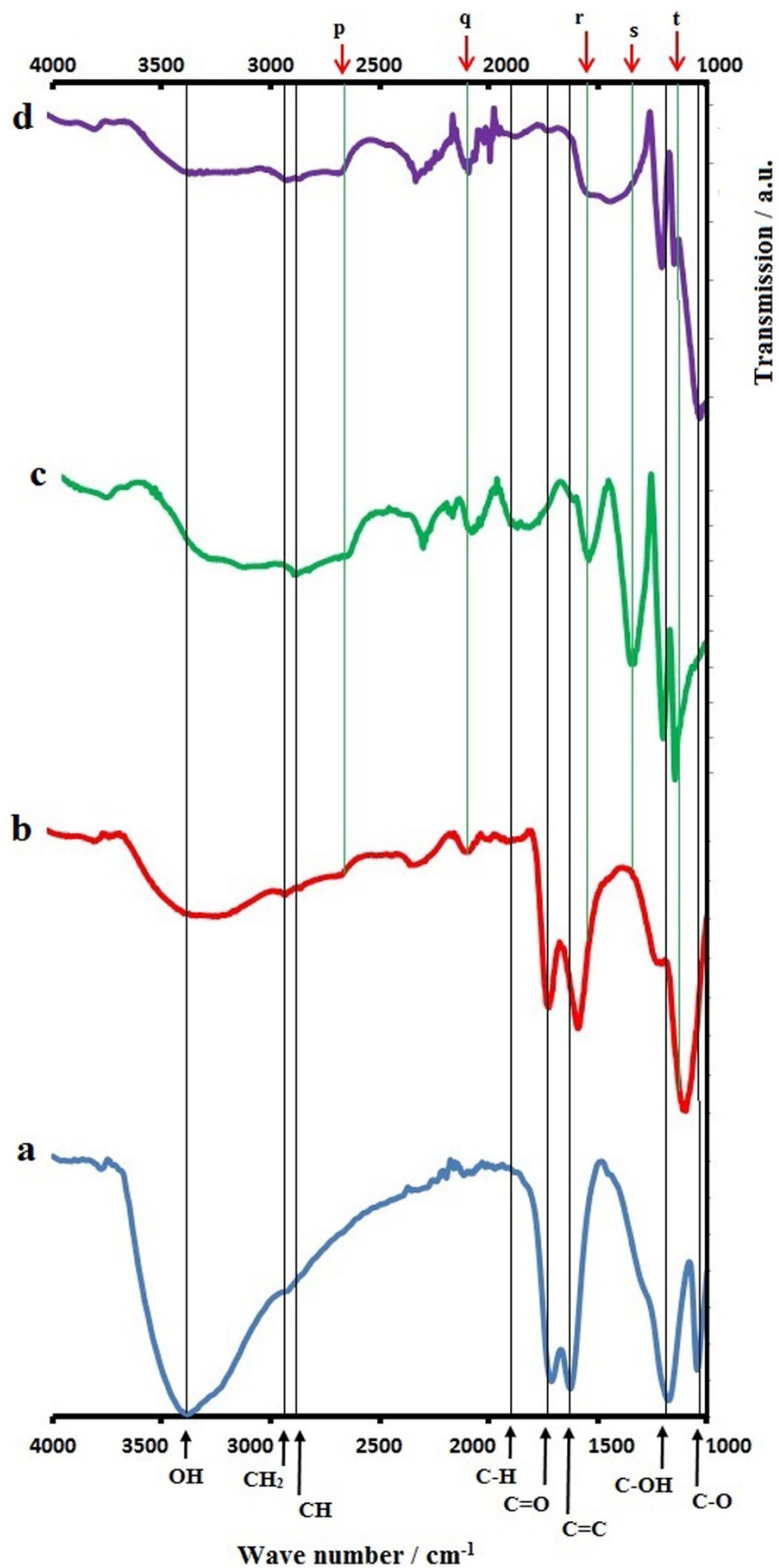


Figure 2 | FTIR of (a) GO (b) GO-MnO₂ before discharge, dried (c) GO-MnO₂ after discharge, not dried (d) ERGO-MnO₂.



C^{25–29}. The FTIR in Fig. 2c shows the appearance of CH₂ and CH groups at approximately 2950 cm⁻¹ and 2870 cm⁻¹, respectively, and the binding energy of the C-H (SI-2b, GO-MnO₂ after discharge) are also assigned close to the C-C at 284.5–285 eV in the C 1s spectrum²⁵. The binding energy at 286.4 eV and 286.1 eV (SI-2a and SI-2b, respectively) are attributed to C-OH^{26–28}, which has the same binding energy as C-O-C^{28,30}. The binding energy at 288.2 eV (SI-2a and SI-2b) is attributed to C=O²⁹, while the binding energy at 289.2 eV (SI-2a) is attributed to O=C-OH^{28,29}. It can be observed (SI-2b) that the peak height and the area under the curve of the C-O peak is increased slightly compared to the C=O peak, which suggests that the electrochemical reduction of C=O to C-O took place during cell discharge, as confirmed by the FTIR result in Fig. 2c. The XPS results also suggest that not all C=O has been reduced to C-O during cell discharge and that some of the GO remains on the surface of the MnO₂. This finding suggests that electro-reduction of the GO to ERGO occur only on the GO surface, consistent with previous reports³¹. A similar trend for the decrease in the peak height and the area under the curve of the C=O peak, and the increase of the peak height and area under the curve of the C-O peak, was observed when GO was reduced with a mixture of argon and hydrogen gases at 200°C, 500°C and 1000°C in a tube furnace³².

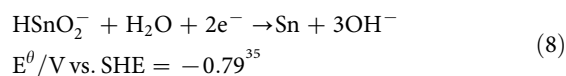
The O 1s spectra for GO-MnO₂ before and after discharge are shown in supporting information (SI-2c and SI-2d), respectively. The binding energies of oxygen bonded Mn atoms (Mn-O and Mn-OH) have been reported to be 530.8 eV and 530.9 eV^{33,34}. Therefore, it can be observed that the binding energy of Mn-O in GO-MnO₂ before and after discharge, (SI-2c and SI-2d respectively) is 531.1 eV. The binding energy of C-O has been reported at 533 eV, while the C=O binding energy, which also has a contribution from O=C-OH³², is 530.6 eV. Thus, the binding energy of C=O at 530.6 eV (SI-2c) together with the binding energy of C-OH at 532.6 eV and at 533 eV (SI-2c and SI-2d, respectively), are in close agreement with previous reports. It can be observed that the C=O peak at 530.5 eV diminishes (SI-2d) when the GO-MnO₂ was discharged as the air cathode, which is due to reduction of the C=O to C-OH. A similar result was also reported when GO was treated at 1000°C with a mixture of argon and hydrogen gases, where a peak binding energy of C=O disappeared due to reduction by hydrogen gas, while the peak binding energy at 533 eV, attributed to C-O, remained in the O 1s spectrum³². When water is introduced to the MnO₂, the binding energy for the absorbed water (O-H₂) is 532.5 eV in the O 1s spectrum^{33,34}. Therefore the peak at 533 eV in the GO-MnO₂ after discharge not dried spectrum (SI-2d) is attributed to the absorbed water molecules. The peak height and area under the curve for the C-OH (532.6 eV) peak are larger compared to the corresponding Mn-O (531.1 eV) in SI-2c. This difference is due to the absence of water in the GO-MnO₂ before discharge, dried cathode. However, the peak height and area under the curve at 533 eV and 531.1 eV (SI-2d) of the C-OH and Mn-O, respectively, are almost identical, which is due to the interaction of absorbed water with Mn (Mn-OH₂), in the GO-MnO₂ after discharge, not dried sample. The XPS spectra of the C 1s and O 1s (SI-2e and SI-2f) of the ERGO-MnO₂ prepared by electrodeposition shows similarities to the C 1s and O 1s spectra of the GO-MnO₂ after discharge (SI-2b and SI-2d, respectively).

Voltammetry, chrono-amperometry and tin-air cell discharge.

The working electrodes (WE) were attached to a cell holder in which the Teflon membrane was exposed to oxygen diffusion from air, while the MnO₂ electro-catalytic surface was exposed to the KOH solution. Voltammetry results from the MnO₂, GO-MnO₂ and ERGO-MnO₂ electrodes in 6 M KOH solution at 5 mV s⁻¹ (supporting information Figure SI-3a and SI-4a) shows that the ORR current of the GO-MnO₂ and ERGO-MnO₂ cathodes are

higher compared to that of the MnO₂ cathode at all potentials. Chrono-amperometry at -0.9 V and the steady-state currents from chrono-amperometry at potentials -0.5, -0.6, -0.7, -0.8, -0.9 and -1.0 V, show that the currents for the GO-MnO₂ and ERGO-MnO₂ cathodes are higher compared to the MnO₂ at all potentials (supporting information SI-3b, SI-3c, SI-4b and SI-4c).

The MnO₂, GO-MnO₂ and ERGO-MnO₂ air cathodes were assembled in an undivided tin-air cell in 6 M KOH. The reactions at the positive and negative electrodes are as follows:



The cell notation for the alkaline tin-air cells can be represented as “Sn|6 M KOH|MnO₂” and “Sn|6 M KOH|GO-MnO₂”. The Sn-MnO₂ and Sn-MnO₂/GO cells are discharged until complete dissolution of the tin negative electrode is reached. The OCP measurements for both cells yielded an average value of 1.20 V, which is close to the standard values calculated in eq. 7 and eq. 8. The chrono-potentiometry plots (SI-5a and SI-5a) at discharge currents of 3, 5, 10, 15, 20, 25 and 30 mA cm⁻² for the Sn-MnO₂ and Sn-MnO₂/GO cells, respectively show that the GO-MnO₂ air cathode gives higher potentials compared to MnO₂ for all discharge currents (SI-5c). From the power density plots (P vs. I) for the tin-air cells with the MnO₂ and GO-MnO₂ air cathodes (SI-5d), it can be observed that the GO-MnO₂ produces higher power density compared to the MnO₂ air cathode. The maximum power density of the Sn-MnO₂ cell is 9.2 mW cm⁻², while the maximum power density of the Sn-GO/MnO₂ cell is more than 13 mW cm⁻² (SI-5d), and both are higher than the power density of 6.8 mW cm⁻² obtained from Zn-air cells³⁶. The current efficiencies that are calculated from weight loss measurements of the tin negative electrode using the Faraday equation ($It = mnF$, $n = 2$) and the discharge profiles (SI-4) are close to 100% for all discharge currents. The charge densities for the dissolution of tin are in the range of 446–449 mAh g⁻¹ for all current densities, which is in accordance with the dissolution of Sn (atomic weight 119) to Sn (II) and is higher than the value of 360 mAh g⁻¹ that has been reported for Zn-air³⁷. The chrono-potentiometry and power density plots of ERGO-MnO₂ (SI-6) also gave higher potentials and power density compared to the bare MnO₂ air cathode. The result of this work and previous works in MFC using MnO₂ graphene composite air cathodes are summarized in the supplementary information (Table SI-1). From the results of other researchers^{11,12} in the supporting information (Table SI-1) the increase of power density compared to the bulk MnO₂ cathode is 1.42 and 1.82 respectively, while in this work, the increase of power density of the GO-MnO₂ and ERGO-MnO₂ compared to the pure MnO₂ cathode, is 1.40 and 1.46 respectively (Table SI-1). The results of other researchers^{11,12} reports the bulk modification of the MnO₂ with graphene and GO respectively, while this work reports the surface modification of the MnO₂ with GO and ERGO.

Electrochemical impedance spectroscopy. EIS was performed on the MnO₂, GO-MnO₂ and ERGO-MnO₂ cathodes in 6 M KOH solution. A two-electrode configuration was used in these EIS experiments, where the MnO₂, ERGO-MnO₂, GO-MnO₂ air cathodes before and after discharge were the WE, while a Hg/HgO electrode in 6M KOH solution was the RE and CE. The Nyquist plots of all four air cathodes are shown in the supplementary information (Figure SI-7). The Nyquist plots show one semi-circle at higher frequencies and a Warburg element at lower frequencies. The $R_f(Q/[R_2W_f])$ equivalent circuit model was found to accurately fit the experimental data, where an excellent agreement was obtained between the experimental data and the simulation of the equivalent



circuit model, and the chi-squared (χ^2) value was minimized to 10^{-4} . The $R_1(Q[R_2W_1])$ equivalent circuit diagrams of the “MnO₂/6 M KOH/Hg-HgO”, “ERGO-MnO₂/6 M KOH/Hg-HgO” and the “GO-MnO₂/6 M KOH/Hg-HgO” systems are similar to the circuit diagram from previous reports^{11,12}.

According to the EIS measurements of the ERGO-MnO₂, GO-MnO₂ and MnO₂ cathodes in 6 M KOH, R_2 is the charge transfer resistance and Q_1 is the CPE for the ORR. The diameter of semicircle represents the charge transfer resistance (Rct) across the electrode-electrolyte interface¹¹. The computer simulations of the EIS experiments indicate that the R_2 (Rct) of the MnO₂, GO-MnO₂ air cathodes before discharge and after discharge, and ERGO-MnO₂ are 310.0 Ohm, 309.0 Ohm, 294.5 Ohm and 294.0 Ohm, respectively. The results of this work and previous report in MFC are shown in the supplementary information (Table SI-2). The charge transfer resistances (Rct) observed for the electrodes fall in the order of MnO₂ nanotubes > Pt/C > MnO₂ nanotubes/GO composite¹². The smaller Rct of the prepared MnO₂/GO composite represents an enhanced reaction rate kinetics with a decreased charge transfer resistance, which is ascribed to the good contact of MnO₂ nanotubes with the carbon support GO and high electrical conductivity of the composite material¹². The result of this work is in good agreement with previous reports^{11,12}.

The Mott-Schottky plot of MnO₂ and GO-MnO₂ in 6M KOH is shown in Fig. 3. From the Mott-Schottky relation:

$$\frac{1}{C_{SCL}^2} = \frac{2}{e\epsilon\epsilon_0 N_D} \left(E - E_{FB} - \frac{kT}{e} \right) \quad (9)$$

Where C_{SCL} is the capacitance of the space charge layer, e is the charge of electron, ϵ_0 is permittivity of free space 8.85×10^{-12} F m⁻¹, ϵ is dielectric constant of MnO₂, E is applied potential, E_{FB} is flat-band potential, N_D is donor density, k is Boltzmann constant, T is Kelvin temperature. The plot of C^{-2} vs E/V for MnO₂ shows a positive slope for both GO-MnO₂ and MnO₂ which is typical for an n-type semiconductor. From the slope of the linear part of the plot close to the flat-band potential ($2/e\epsilon\epsilon_0 N_D$), shows that the slope for GO-MnO₂ is lower than MnO₂. This suggests that the charge carrier (electron for n-type semiconductor) density is larger for the GO-MnO₂ compared to MnO₂.

Discussion

From the FTIR spectra, it can be concluded that the GO on the MnO₂ cathode surface was reduced to electrochemically reduced graphene oxide (ERGO) during cell discharge in 6M KOH, and this finding is in accordance with the electrochemical reduction of GO to ERGO in concentrated alkaline solution³¹. Tin-air discharge, LSV and chrono-

amperometry results confirm the increased electro-catalytic effect of the GO-MnO₂ cathode toward the ORR compared to the MnO₂ without the GO.

In the EIS results, the smaller R_2 (Rct) of the GO-MnO₂ air cathode after discharge is due to the reduction of GO to ERGO on the MnO₂ surface during cell discharge. Therefore, the presence of ERGO is responsible for the lower R_2 of the GO-MnO₂ air cathode after discharge. It can be observed that ERGO has lower interfacial charge transfer resistance compared to GO due to the higher electrical conductivity of ERGO compared to GO³⁸, which is consistent with previous work³⁹. Therefore, during cell discharge, some of the GO is reduced to ERGO, and this decreases the interfacial charge transfer resistance of the GO-MnO₂ cathode after discharge. The EIS simulation results show only a small difference between the R_2 of the MnO₂ and GO-MnO₂ air cathodes before discharge, while the GO-MnO₂ air cathode after discharge has the smallest R_2 value. However, voltammetry, chrono-amperometry and the tin-air cell discharge results clearly show higher currents and higher power densities for the GO-MnO₂ compared to the MnO₂ air cathode. The ORR mechanisms on the MnO₂ electro-catalyst in alkaline solution are given in eq. 3 to eq. 6. The charge transfer resistance (R_2) is the resistance against the interfacial electron transfer process that occurs across the air cathode-KOH electrolyte interface for the ORR. Therefore, eq. 3 and eq. 6 are related to the rate of the electron transfer process, and R_2 depends only on eq. 3 and eq. 6. However, the electron transfer steps in eq. 3 and eq. 6 are fast reactions and thus are not rate determining steps in the ORR. Hence, the R_2 values of the MnO₂ and GO-MnO₂ air cathodes before and after discharge cannot explain the increased currents and power densities for the GO-MnO₂ air cathode.

The overall current for the ORR depends on the reaction mechanisms proposed in eq. 3 to eq. 6. The chemical step in eq. 5, where the electron is excited from the valence band to the conduction band of the MnO₂ electro-catalyst and is then donated to the adsorbed oxygen molecule, is the slowest step. This step has been proposed to be the rate determining step^{7,9}, and therefore, this step controls the overall current of the ORR. An increase in electrical conductivity in graphene composite materials has been reported⁴⁰, which is due to a lowering of the band-gap of the composite materials in the presence of graphene. The presence of ERGO on the surface of polypyrrole nanofibers, which increases the electrical conductivity of the nanofibers by decreasing the band-gap of polypyrrole, has been proposed¹⁶. There are two possible reasons for the increased currents and power densities of the GO-MnO₂ air cathode. First, the GO and ERGO are efficient electro-catalysts for the ORR, and their presence on the MnO₂ surface provides a high surface area for the ORR to proceed. Second, the electron rich GO and ERGO on the MnO₂ surface increase the rate determining step of the ORR. The increased electro-catalytic effect of the GO-MnO₂ cathode for the ORR, is due to enhanced electron donation from the MnO₂ electro-catalyst to the adsorbed oxygen molecule in the rate determining step (eq. 5). Given the presence of electron rich GO and ERGO on the surface of MnO₂, electrons are transferred efficiently from the GO and ERGO to the conduction band of the MnO₂, as shown in Fig. 4, thus increasing the rate of this step (eq. 5). Therefore, the presence of GO and ERGO on the MnO₂ surface can result in faster electron donation in eq. 5, thus increasing the speed of the rate determining step of the ORR. From the Mott-Schottky results, the larger electron density in ERGO-MnO₂ is responsible for the larger electron donation effect in the rate determining step for the ORR. Thus the presence of ERGO acts like an electron pump for MnO₂ to accelerate the ORR.

Furthermore, at faster discharge rates, at currents higher than 15 mA cm⁻², GO-MnO₂ and provides higher power density than MnO₂ (SI-5d and SI-6d). This effect is also due to the faster donation of electrons from the GO to MnO₂ (Fig. 4) compared to the excitation process in eq. 5. The MnO₂ air cathode provides lower power densi-

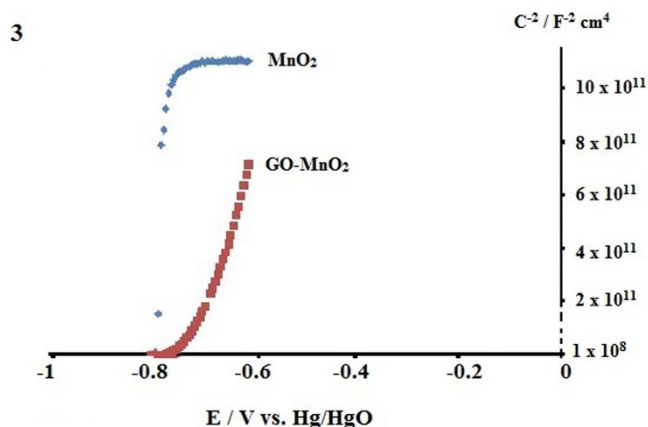


Figure 3 | Mott-Schottky plots of MnO₂ and GO-MnO₂.

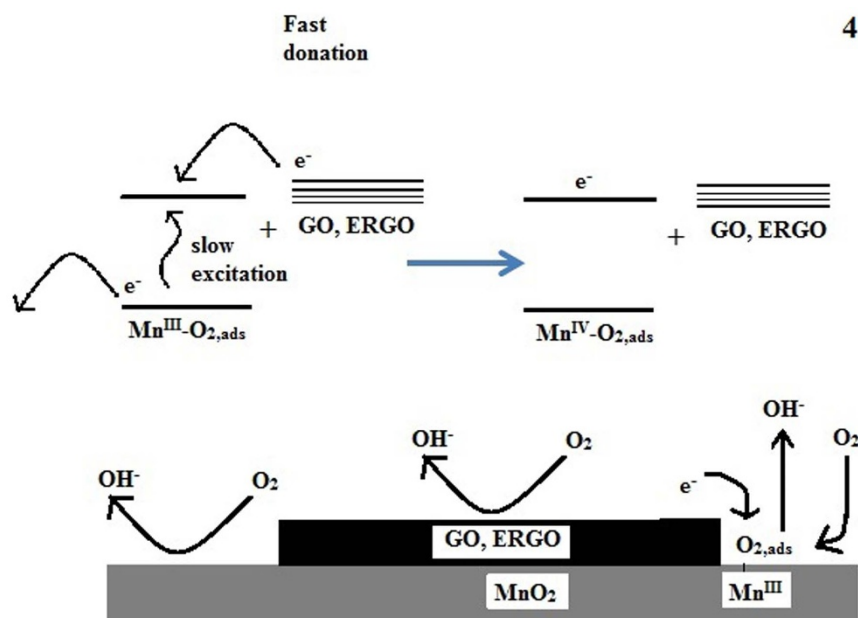


Figure 4 | Diagram of the electron donating effect of GO and ERGO on MnO_2 adsorbed oxygen $\text{Mn}^{3+}\text{-O}_{2,\text{ads}}$.

ties at higher discharge rates due to the slower electron excitation process and is thus unable to meet high demands at discharge rates that are faster than 15 mA cm^{-2} . Given the presence of GO on the MnO_2 surface, high demands at discharge rates that are faster than 15 mA cm^{-2} can be met by faster electron donation from the GO (and ERGO) to the MnO_2 (Fig. 4), and thus, the GO- MnO_2 and ERGO- MnO_2 cathodes provide higher powder densities compared to the bare MnO_2 cathode.

Methods

Synthesis. All chemicals were from Sigma Aldrich. The GO powder was prepared using a modified Hummers' method. The GO powder was dispersed in a beaker filled with distilled water and sonicated for 5 hours until the final concentration was 0.3 mg cm^{-3} . The air cathode was catalytic MnO_2 mixed with small amounts of carbon black to increase its conductivity. The powders were pressed onto a nickel mesh current collector, with one side attached to a Teflon membrane that was permeable to air but not to the electrolyte. The air cathode was placed in a jar with the MnO_2 catalytic layer facing upwards. The GO dispersion was poured into a jar and evaporated overnight at 50°C in an oven (supplementary information Figure SI-8). In the electrodeposition of GO on the MnO_2 cathode, GO powder (7 mg dm^{-3}) was dispersed in 0.1 M phosphate buffer solution (K_2HPO_4 and KH_2PO_4) at pH 7.2 and sonicated for 5 hours. The electrodeposition of GO on the surface of MnO_2 substrate was performed by cyclic voltammetry in a single compartment cell in 4 voltammetric scans. A saturated calomel electrode (SCE) was used as the reference, while a platinum foil with 2 cm^2 surface area was the counter electrode. The potential range applied was from 0.0 to -1.5 V with the scan rate of 1 mV s^{-1} . The Mott-Schottky experiment was performed using a two electrode system, in 6 M KOH , with the MnO_2 and GO- MnO_2 electrodes as the WE, and the Hg/HgO as the reference and counter electrodes, at a constant frequency of 1000 Hz .

Characterization. The evaporated GO layers on the MnO_2 air cathode (GO- MnO_2) and electrodeposited ERGO- MnO_2 were characterized using Fourier transformed infrared (FTIR) spectroscopy and field emission scanning electron microscopy (FESEM). The FTIR and FESEM instruments were Spectrum 400 and Quanta 200F, respectively. X-ray photoelectron spectroscopy (XPS) was conducted using a Kratos analytical axis ultra instrument with an Al K_α radiation source of 253.6 eV . Linear scan voltammetry (LSV), chrono-amperometry and electrochemical impedance spectroscopy (EIS) were performed using a potentiostat/galvanostat Autolab PGSTAT-302N from Ecochemie (Utrecht, Netherlands). LSV and chrono-amperometry were performed using a single compartment cell, with a mercury oxide (Hg/HgO) as the reference electrode (RE) and a graphite rod as the counter electrode (CE), while a two-electrode configuration was used in the EIS experiments. The EIS measurements were performed over a frequency range of 100 kHz to 10 mHz , with the acquisition of 10 points per decade, with a signal amplitude of 5 mV around the open circuit potential (OCP). The impedance spectra were analyzed by fitting the experimental results to equivalent circuits using a non-linear least-square fitting procedure with the chi-squared value minimized to 10^{-4} . The OCP and tin-air cell discharge experiments were conducted using a Won-A-Tech WBCS 3000 (Korea Republic) battery cyclers system. Tin metal foils with an area of 2 cm^2 were used as the

negative electrode in a 6 M KOH solution for the tin-air cell discharge experiments. The diameters of the MnO_2 and GO- MnO_2 positive electrodes were 0.9 cm in all experiments. The diagrams of the air cathode and the cell casing are described elsewhere⁴¹. The discharge capacity in mAh g^{-1} of the alkaline tin-air cell was measured from the chrono-potentiometry diagram and the weight loss of the tin negative electrode after cell discharge. All experiments were performed at room temperature, 27°C .

- Sun, B. *et al.* Graphene nanosheets as cathode catalysts for lithium-air batteries with an enhanced electrochemical performance. *Carbon* **50**, 727–733 (2012).
- Xiao, J. *et al.* Hierarchically porous graphene as a lithium-air battery electrode. *Nano Lett.* **11**, 5071–5078 (2011).
- Qu, L., Liu, Y., Baek, J. B. & Dai, L. Nitrogen-doped graphene as efficient metal-free electrocatalyst for oxygen reduction in fuel cells. *ACS Nano* **4**, 1321–1326 (2010).
- Byon, H. R., Suntivich, J. & Horn, Y. S. Graphene-based non-noble metal catalysts for oxygen reduction reaction in acid. *Chem. Mater.* **23**, 3421–3428 (2011).
- Gong, K., Yu, P., Su, L., Xiong, S. & Mao, L. Polymer-assisted synthesis of manganese dioxide/carbon nanotube nanocomposite with excellent electrocatalytic activity toward reduction of oxygen. *J. Phys. Chem. C* **111**, 1882–1887 (2007).
- Mao, L. *et al.* Mechanistic study of the reduction of oxygen in air electrode with manganese oxides as electrocatalysts. *Electrochim. Acta* **48**, 1015–1021 (2003).
- Lima, F. H. B., Calegario, M. L. & Ticianelli, E. A. Investigations of the catalytic properties of manganese oxides for the oxygen reduction reaction in alkaline media. *J. Electroanal. Chem.* **590**, 152–160 (2006).
- Wang, S., Yu, D., Dai, L., Chang, D. W. & Baek, J.-B. Polyelectrolyte-functionalized graphene as metal-free electrocatalysts for oxygen reduction. *Nano Lett.* **5**, 6202–6209 (2011).
- Lima, F. H. B., Calegario, M. L. & Ticianelli, E. A. Electrocatalytic activity of manganese oxides prepared by thermal decomposition for oxygen reduction. *Electrochim. Acta* **52**, 3732–3738 (2007).
- Yang, Y., Shi, M., Li, Y.-S. & Fu, Z.-W. MnO_2 -graphene composite air electrode for rechargeable Li-air batteries. *J. Electrochem. Soc.* **159**, A1917–A1921 (2012).
- Wen, Q. *et al.* MnO_2 -graphene hybrid as an alternative cathodic catalyst to platinum in microbial fuel cells. *J. Power Sources* **216**, 187–191 (2012).
- Gnanakumar, G., Awan, Z., Nahm, K. S. & Xavier, J. S. Nanotubular MnO_2 /graphene oxide composites for the application of open air-breathing cathode microbial fuel cells. *Biosens. Bioelectronics* **53**, 528–534 (2014).
- Qian, Y., Lu, S. & Gao, F. Synthesis of manganese dioxide/reduced graphene oxide composites with excellent electrocatalytic activity toward reduction of oxygen. *Mater. Lett.* **65**, 56–58 (2011).
- Chen, L., Tang, Y., Wang, K., Liu, C. & Luo, S. Direct electrodeposition of reduced graphene oxide on glassy carbon electrode and its electrochemical application. *Electrochem. Commun.* **13**, 133–137 (2011).
- Zhou, M. *et al.* Controlled synthesis of large-area and patterned electrochemically reduced graphene oxide films. *Chem-Eur. J.* **15**, 6116–6120 (2009).
- Mahmoudian, M. R., Alias, Y. & Basirun, W. J. The electrical properties of a sandwich of electrodeposited polypyrrole nanofibers between two layers of reduced graphene oxide nanosheets. *Electrochim. Acta* **72**, 53–60 (2012).



17. Jiang, Z., Jin, J., Xiao, C. & Li, X. Effect of surface modification of carbon black (CB) on the morphology and crystallization of poly(ethylene terephthalate)/CB masterbatch. *Colloids Surf. A* **395**, 105–115 (2012).
18. Yang, R., Wang, Z., Dai, L. & Chen, L. Synthesis and characterization of single-crystalline nanorods of α -MnO₂ and γ -MnOOH. *Mater. Chem. Phys.* **93**, 149–153 (2005).
19. Pramod, K., Sharma, M. S. & Whittingham, M. S. The role of tetraethyl ammonium hydroxide on the phase determination and electrical properties of γ -MnOOH synthesized by hydrothermal. *Mater. Lett.* **48**, 319–323 (2001).
20. Kohler, T., Armbruster, T. & Libowitzky, E. Hydrogen bonding and Jahn-Teller distortion in groutite, α -MnOOH, and manganite, γ -MnOOH, and their relations to the manganese dioxides Ramsdellite and Pyrolusite. *J. Solid State Chem.* **133**, 486–500 (1997).
21. Ananth, M. V., Pethkar, S. & Dakshinamurthi, K. Distortion of MnO octahedra and electrochemical activity of Nstutite-based MnO polymorphs for alkaline electrolytes-an FTIR study. *J. Power Sources* **75**, 278–282 (1998).
22. Lerf, A., He, H., Forster, M. & Klinowski, J. Structure of graphite oxide revisited. *J. Phys. Chem. B* **102**, 4477–4482 (1998).
23. Young, C. W., DuVall, R. B. & Wright, N. Characterization of benzene ring substitution by infrared spectra. *Anal. Chem.* **23**, 709–714 (1951).
24. Whiffen, D. H. Infra-red summation bands of the out-of-plane C-H bending vibrations of substituted benzene compounds. *Spectrochim. Acta* **7**, 253–263 (1956).
25. Yumitori, S. Correlation of C1s chemical state intensities with the O1s intensity in the XPS analysis of anodically oxidized glass-like carbon samples. *J. Mater. Sci.* **35**, 139–146 (2000).
26. Becerril, H. A. *et al.* Evaluation of solution-processed reduced graphene oxide films as transparent conductors. *ACS Nano* **2**, 463–470 (2008).
27. Stankovich, S. *et al.* Stable aqueous dispersions of graphitic nanoplatelets via the reduction of exfoliated graphite oxide in the presence of poly(sodium 4-styrenesulfonate). *J. Mater. Chem.* **16**, 155–158 (2006).
28. Stankovich, S. *et al.* Synthesis of graphene-based nanosheets via chemical reduction of exfoliated graphite oxide. *Carbon* **45**, 1558–1565 (2007).
29. Park, S. *et al.* Graphene oxide papers modified by divalent ions-enhancing mechanical properties via chemical cross-linking. *ACS Nano* **2**, 572–578 (2008).
30. Kozlowski, C. & Sherwood, P. M. A. X-ray photoelectron spectroscopic studies of carbon-fiber surfaces, Part 4, the effect of electrochemical treatment in nitric acid. *J. Chem. Soc. Faraday Trans.* **80**, 2099–2107 (1984).
31. Basirun, W. J., Sookhajian, M., Baradaran, S., Mahmoudian, M. R. & Ebadi, M. Solid-phase electrochemical reduction of graphene oxide films in alkaline solution. *Nanoscale Res. Lett.* **8**, 397 (2013).
32. Yang, D. *et al.* Chemical analysis of graphene oxide films after heat and chemical treatments by X-ray photoelectron and micro-Raman spectroscopy. *Carbon* **47**, 145–152 (2009).
33. Nesbitt, H. W. & Banerjee, D. Interpretation of XPS Mn(2p) spectra of Mn oxyhydroxides and constraints on the mechanism of MnO₂ precipitation. *Am. Mineral.* **83**, 305–315 (1998).
34. Pang, S. U. & Anderson, M. A. Novel electrode materials for electrochemical capacitors: Part II. Material characterization of sol-gel-derived and electrodeposited manganese dioxide thin films. *J. Mater. Res.* **15**, 2096–2106 (2000).
35. Jiang, R. Combinatorial electrochemical cell array for high throughput screening of micro-fuel-cells and metal/air batteries. *Rev. Sci. Instrum.* **78**, 1–7 (2007).
36. Mohamad, A. A. Zn/gelled 6M KOH/O₂ zinc-air battery. *J. Power Sources* **159**, 752–757 (2006).
37. Yang, H., Cao, Y., Ai, X. & Xiao, L. Improved discharge capacity and suppressed surface passivation of zinc anode in dilute alkaline solution using surfactant additives. *J. Power Sources* **128**, 97–101 (2004).
38. Eda, G., Fanchini, G. & Chhowalla, M. Large-area ultrathin films of reduced graphene oxide as a transparent and flexible electronic material. *Nature Nanotech.* **3**, 270–274 (2008).
39. Ambrosi, A., Bonanni, A., Sofer, Z., Cross, J. S. & Pumera, M. Electrochemistry at chemically modified graphenes. *Chem. Eur. J.* **17**, 10763–10770 (2011).
40. Stankovich, S. *et al.* Graphene-based composite materials. *Nature* **442**, 282–286 (2006).
41. Othman, R., Basirun, W. J., Yahya, A. H. & Arof, A. K. Hydroponics gel as a new electrolyte gelling agent for alkaline zinc-air cells. *J. Power Sources* **103**, 34–41 (2001).

Acknowledgments

The authors would like to thank University Malaya and Ministry of Higher Education for providing financial assistance under grant numbers FP033 2013A, PG015-2013A and PG-084-2013A for this work.

Author contributions

W.J.B. wrote the paper. S.B., M.S., R.Y., H.G. and S.M. prepared the GO and ERGO electrodes. M.R.M. and M.E. performed the EIS experiments. Z.E. ran the FTIR, XPS spectra and the other electrochemical experiments. All authors reviewed the revised manuscript and approved the submission.

Additional information

Supplementary information accompanies this paper at <http://www.nature.com/scientificreports>

Competing financial interests: The authors declare no competing financial interests.

How to cite this article: Basirun, W.J. *et al.* Graphene oxide electrocatalyst on MnO₂ air cathode as an efficient electron pump for enhanced oxygen reduction in alkaline solution. *Sci. Rep.* **5**, 9108; DOI:10.1038/srep09108 (2015).



This work is licensed under a Creative Commons Attribution 4.0 International License. The images or other third party material in this article are included in the article's Creative Commons license, unless indicated otherwise in the credit line; if the material is not included under the Creative Commons license, users will need to obtain permission from the license holder in order to reproduce the material. To view a copy of this license, visit <http://creativecommons.org/licenses/by/4.0/>